^{11}C-Choline Pharmacokinetics in Recurrent Prostate Cancer

Milan Grkovski[1], Karem Gharzeddine*[2], Peter Sawan*[2], Heiko Schöder[2,3], Laure Michaud[2], Wolfgang A. Weber[2–4], and John L. Humm[1]

[1]Department of Medical Physics, Memorial Sloan Kettering Cancer Center, New York, New York; [2]Department of Radiology, Memorial Sloan Kettering Cancer Center, New York, New York; [3]Molecular Imaging and Therapy Service, Memorial Sloan Kettering Cancer Center, New York, New York; and [4]University Hospital Klinikum Rechts der Isar, Technical University of Munich, Munich, Germany

The aim of this study was to investigate the value of pharmacokinetic modeling for quantifying ^{11}C-choline uptake in patients with recurrent prostate cancer. **Methods:** In total, 194 patients with clinically suspected recurrence of prostate cancer underwent ^{11}C-choline dynamic PET over the pelvic region (0–8 min), followed by a 6-min static acquisition at about 25 min after injection. Regions of interest were drawn over sites of disease identified by a radiologist with experience in nuclear medicine. ^{11}C-choline uptake and pharmacokinetics were evaluated by SUV, graphical analysis (Patlak plot; K_i^P), and 1- and 2-compartment pharmacokinetic models (K_1, K_1/k_2, k_3, k_4, and the macro parameter K_i^C). Twenty-four local recurrences, 65 metastatic lymph nodes, 19 osseous metastases, and 60 inflammatory lymph nodes were included in the analysis, which was subsequently repeated for regions of interest placed over the gluteus maximus muscle and adipose tissue as a control. **Results:** SUV_{mean} and K_i^P were 3.60 ± 2.16 and 0.28 ± 0.22 min^{-1} in lesions, compared with 2.11 ± 1.33 and 0.15 ± 0.10 min^{-1} in muscle and 0.26 ± 0.07 and 0.02 ± 0.01 min^{-1} in adipose tissue. According to the Akaike information criterion, the 2-compartment irreversible model was most appropriate in 85% of lesions and resulted in a K_1 of 0.79 ± 0.98 min^{-1} (range, 0.11–7.17 min^{-1}), a K_1/k_2 of 2.92 ± 3.52 (range, 0.31–20.00), a k_3 of 0.36 ± 0.30 min^{-1} (range, 0.00–1.00 min^{-1}) and a K_i^C of 0.28 ± 0.22 min^{-1} (range, 0.00–1.33 min^{-1}). The Spearman ρ between SUV and K_i^P, between SUV and K_i^C, and between K_i^P and K_i^C was 0.94, 0.91, and 0.97, respectively, and that between SUV and K_1, between SUV and K_1/k_2, and between SUV and k_3 was 0.70, 0.44, and 0.33, respectively. Malignant lymph nodes exhibited a higher SUV, K_i^P, and K_i^C than benign lymph nodes. **Conclusion:** Although ^{11}C-choline pharmacokinetic modeling has potential to uncouple the contributions of different processes leading to intracellular entrapment of ^{11}C-choline, the high correlation between SUV and both K_i^P and K_i^C supports the use of simpler SUV methods to evaluate changes in ^{11}C-choline uptake and metabolism for treatment monitoring.

Key Words: ^{11}C-choline; dynamic PET; kinetic modeling; prostate cancer; metastasis

J Nucl Med 2018; 59:1672–1678
DOI: 10.2967/jnumed.118.210088

Prostate cancer (PCa) is one of the most commonly diagnosed cancers in men worldwide. It is estimated that 164,690 new cases of PCa will be diagnosed and that 29,430 men will die of the disease in the United States in 2018 (*1*). Despite initial treatment with curative intent, biochemical recurrences, defined as an increase in prostate-specific antigen (PSA) level, occur in more than 25% of cases.

^{11}C-choline is a PET radiopharmaceutical for the detection and localization of recurrent PCa, with its Food and Drug Administration approval being based primarily on its ability to detect disease not visualized with conventional imaging. Choline is a precursor of phospholipids, major structural components of the plasma membrane, and as such is necessary for membrane synthesis and cell division (*2*). It is predominantly transported into cells via high-affinity sodium-dependent choline transporters, phosphorylated by choline kinase (which is overexpressed in many malignant tumors, including PCa), and incorporated into phospholipids such as phosphatidylcholine. Choline also plays a role in cell proliferation by modulating transmembrane signaling (*3*).

Meta-analysis of PCa patients with biochemical recurrence undergoing ^{11}C-choline PET (12 studies, 1,055 patients) by Umbehr et al. reported a pooled sensitivity of 85% and a pooled specificity of 88% (*4*). Evangelista et al. reviewed the use of ^{11}C-choline PET in biochemical relapse of PCa (19 studies, 1,555 patients), reporting a pooled sensitivity of 86% and a pooled specificity of 93% for all sites of disease (*5*). More recently, Fanti et al., evaluating ^{11}C-choline in recurrent PCa (29 studies, 2,686 patients), reported 89% pooled sensitivity and 89% pooled specificity (*6*). On the other hand, Ren et al., performing a meta-analysis of ^{18}F-fluciclovine PET/CT (6 studies, 251 patients) in the diagnosis of recurrent PCa, reported 87% pooled sensitivity and 66% pooled specificity (*7*); however, the specificities for extraprostatic disease may be higher than the meta-analysis suggests (*8*). ^{11}C-choline is relatively insensitive in patients who have biochemically recurrent PCa after surgery with PSA values of less than 2 ng/mL. A recent study comparing ^{68}Ga-labeled PSMA-11 and ^{11}C-choline PET for detection of PCa metastases concluded that ^{68}Ga-labeled PSMA-11 PET exhibited significantly higher uptake and a significantly higher detection rate than ^{11}C-choline PET in the subgroup of patients with PSA levels below 1 ng/mL (*9*). However, ^{11}C-choline PET/CT is attractive for monitoring tumor response to therapy in patients with metastatic PCa. ^{11}C-choline uptake reflects a basic metabolic process of the cancer cells that is not directly regulated by androgen signaling. In contrast, PSMA expression is negatively regulated by androgens.

Received Feb. 26, 2018; revision accepted Mar. 23, 2018.
For correspondence or reprints contact: Milan Grkovski, Department of Medical Physics, Memorial Sloan Kettering Cancer Center, 1275 York Ave., New York, NY 10065.
E-mail: grkovskm@mkscc.org
*Contributed equally to this work.
Published online Apr. 6, 2018.

During androgen deprivation therapy, uptake of PSMA ligands may therefore increase at least temporarily in responding tumors (*10*). Quantitative analysis of PSMA PET scans during androgen deprivation therapy, a cornerstone of all PCa therapy, may therefore be challenging.

To use ^{11}C-choline PET/CT for monitoring tumor response, it is important to provide quantitative measures of tracer uptake. The simplest approach to assess ^{11}C-choline uptake is the calculation of SUV at a fixed time. For ^{18}F-FDG PET, multiple studies have shown that SUVs and SUV changes during therapy correlate well with glucose metabolic rates determined from tracer kinetic modeling (*11*). Therefore, SUVs are now routinely used to monitor changes in glucose metabolic activity (*12*). However, there are only a few similar analyses for ^{11}C-choline PET/CT.

The aim of the current study was to explore the potential added benefit of pharmacokinetic modeling for quantifying PET uptake in a large cohort of patients with recurrent PCa using a radiotracer that has already been extensively applied in a clinical setting. We also sought to determine how well SUVs from static PET scans correlate with ^{11}C-choline uptake rates derived from dynamic scans. Furthermore, we investigated whether pharmacokinetic modeling of ^{11}C-choline biodistribution can facilitate better differentiation of tumor-involved and inflammatory lymph nodes.

MATERIALS AND METHODS

Patient Selection

All patients participated in an institutional review board–approved expanded access study (protocol 15-117) and gave written informed consent to the examination and use of anonymous data for research and publication purposes. There were 4 inclusion criteria. The first was biopsy-proven adenocarcinoma of the prostate initially treated with curative intent. The second, biochemical recurrence, was defined as a PSA level of at least 0.2 ng/mL in at least 2 sequential tests for patients treated with prostatectomy; a PSA level of at least 0.2 ng/mL above the posttherapy nadir for patients treated with radiation therapy, brachytherapy, or cryotherapy; or a PSA level of at least 0.2 ng/mL above the most recent therapy nadir for patients who received additional treatment in the setting of recurrence. The third inclusion criterion was negative or inconclusive findings on standard-of-care imaging studies (e.g., CT, MRI, conventional bone scintigraphy, or ^{111}In-capromab pendetide scintigraphy), and the fourth was an age of at least 18 y. In total, 194 patients were included in the study between March 2016 and December 2016.

PET/CT Imaging

^{11}C-choline was synthesized on-site by *N*-^{11}C-methylation of dimethylethanolamine in ethanol with ^{11}C-methyl iodide and isolated by solid-phase extraction on a cation-exchange cartridge. Residual dimethylethanolamine and ^{11}C-methyl iodide were removed from the cartridge by rinsing it with ethanol and water, and the remaining purified product was eluted with sterile isotonic saline through a sterilizing filter into the final product vial.

The patients fasted for at least 4 h before the scan and were encouraged to void before and after imaging. Concurrent with an intravenous bolus injection of 370–740 MBq of ^{11}C-choline, the patients underwent dynamic PET on a Discovery 690 or Discovery 710 PET/CT scanner (GE Healthcare) over the pelvic region (0–8 min; binned into 6 × 10 s, 4 × 30 s, and 5 × 60 s). This scan was followed by a whole-body scan lasting about 18 min after injection (not used for the purpose of pharmacokinetic modeling) and a 6-min static acquisition at about 26 min after injection, focused over the pelvic region. The CT images acquired immediately before the PET scan were performed with 120 kVp, 80 mAs, and a 3.8-mm slice thickness. All PET emission data were corrected for attenuation, scatter, and random events and then iteratively reconstructed into a 128 × 128 × 47 matrix (voxel dimensions, 5.46 × 5.46 × 3.27 mm) using the ordered-subset expectation-maximization algorithm provided by the manufacturer.

Image Analysis

The images were analyzed in PMOD, version 3.604 (PMOD Technologies GmbH). Regions of interest were manually drawn over sites of disease and inflammatory lymph nodes that were identified by a radiologist with experience in PET/CT imaging and nuclear medicine, on the late-time-point 6-min static PET scan. For this purpose, the PET scans were fused with their corresponding CT scans to provide anatomic information. Uptake in inguinal lymph nodes was considered inflammatory because the inguinal nodes are not in the lymphatic drainage system of the prostate (*13*).

^{11}C-choline uptake was measured by the SUV_{mean} within the region of interest. Graphical analysis was performed to calculate the Patlak slope (K_i^P). In addition, irreversible and reversible 1-compartment (1T1K and 1T2K, respectively) and 2-compartment (2T3K and 2T4K, respectively) pharmacokinetic models were investigated to calculate the kinetic rate constants K_1, K_1/k_2, k_3, and k_4. In all 4 compartment models, the blood volume fraction was also fitted. Additionally, a macro parameter derived from compartmental analysis (K_i^C) was calculated and compared with the K_i^P. K_i^C is a unidirectional uptake rate constant defined as

$$K_i^C = \frac{K_1 k_3}{k_2 + k_3}. \quad \text{Eq. 1}$$

^{11}C-choline equilibration time, T^*, was calculated as

$$T^* = 7 \cdot \frac{\ln 2}{(k_2 + k_3)} \quad \text{Eq. 2}$$

and represents the time after which unbound ^{11}C-choline has reached more than 99% of its final ratio relative to blood. The input function was derived from the dynamic PET images, segmenting the femoral artery on the early frame with the highest image intensity by selecting approximately the 200 hottest voxels. Image-derived input function time–activity curves were defined using the available temporal data (i.e., the first 8 min of the dynamic acquisition and the last 6 min of the static frame) and fitted with a triphasic exponential function. The target activity concentration at each time frame was weighed by

$$w_i = \frac{1}{\sigma_i^2}, \sigma_i = c\sqrt{\left(\frac{AC(t_i)}{\Delta t_i \times e^{-\lambda t_i}}\right)}, \quad \text{Eq. 3}$$

where c is the scaling factor, Δt_i is the frame duration, $AC(t_i)$ is the decay-corrected activity concentration measured at midframe time t_i, and λ is the isotope decay constant (ln2 divided by half-life). Because metabolite counts were not acquired on a patient-by-patient basis, population-wise metabolite correction was applied using previously reported values (*14,15*). The Akaike information criterion as implemented in PMOD was used to determine the most appropriate compartmental model (*16*). The correlation between investigated metrics was analyzed using the Spearman ρ. Metrics were compared between groups using the unpaired 2-tailed Student *t* test. A *P* value of less than 0.05 was assumed to represent statistical significance.

RESULTS

According to the National Comprehensive Cancer Network guidelines, the pretreatment risk categories for the 194 patients

were category I for 1 patient, IIA for 28 patients, IIB for 23 patients, III for 71 patients, and IV for 58 patients. In 13 patients, the risk category could not be calculated. In total, 48% of patients (94/194) had positive findings on the whole-body ^{11}C-choline scan, indicating local recurrence in 12% of patients (24/194), lymph node metastasis in 32% of patients (62/194), and bone metastasis in 14% of patients (27/194). Four of 27 patients with bone metastases also exhibited lymph node metastases. The median PSA and Gleason score were 2.5 ng/mL (range, 0.3–82.9 ng/mL) and 7 (range, 6–10), respectively. The detection rate for local recurrence or metastatic disease varied by PSA value: 12% (6/49) for a PSA value of less than 0.5 ng/mL, 34% (11/32) for 0.5–1.0 ng/mL, 68% (21/31) for 1.0–2.0 ng/mL, and 68% (56/82) for more than 2.0 ng/mL. Detection according to the National Comprehensive Cancer Network risk category was 100% for category I (1/1), 64% for IIA (18/28), 30% for IIB (7/23), 48% for III (34/71), 47% for IV (27/58), and 54% unknown (7/13).

Twenty-one patients had lesions outside the 15.7-cm axial field of view of the dynamic scan. Pharmacokinetic modeling was performed for the remaining 73 patients, with 108 malignant lesions (24 local recurrences, 65 lymph node metastases, and 19 osseous metastases) being included in the analysis. For these patients, the pharmacokinetic modeling was also conducted for regions of interest placed over gluteus maximus muscle and adipose tissue. Additionally, 60 inguinal lymph nodes with probable inflammation were analyzed in 26 patients. Biopsies were performed in 33 of the 73 patients for whom pharmacokinetic modeling was performed. In all 33 patients, the results were positive. The biopsy results were negative in all 3 patients for whom biopsies were performed in inguinal lymph nodes.

SUV_{mean} and K_i^P were 3.60 ± 2.16 and 0.26 ± 0.17 min^{-1} in malignant lesions, compared with 1.63 ± 0.70 and 0.11 ± 0.04 min^{-1} in inflammatory lymph nodes, 1.02 ± 0.40 and 0.07 ± 0.03 min^{-1} in muscle, and 0.26 ± 0.07 and 0.02 ± 0.01 min^{-1} in adipose tissue (Table 1). Malignant lymph nodes were found to have a significantly higher SUV, K_i^P, and K_i^C than inflammatory lymph nodes (Table 1, $P < 0.01$). ^{11}C-choline equilibration was sufficiently fast relative to the total scan duration in all lesions and inflammatory lymph nodes.

According to the Akaike information criterion as implemented in PMOD, the 2T3K model was the most appropriate in 85% of lesions, with the 1T1K and 1T2K models being the most appropriate in the remaining 15% of lesions. The Akaike information criterion values for the 1T1K, 1T2K, 2T3K, and 2T4K models were 147 ± 16, 140 ± 15, 127 ± 12, and 132 ± 18, respectively. The pharmacokinetic modeling results for all analyzed tissues, as calculated with the 2T3K model, are summarized in Table 1. A significantly higher SUV, K_i^P, K_i^C, K_1, K_i/k_2, and k_3 were observed in malignant lesions than in inflammatory lymph nodes, with values for muscle and adipose tissue being lower still. The ^{11}C-choline distribution volume (approximated by K_1/k_2) was around unity in inflammatory lymph nodes and muscle tissue; however, it was slightly lower in adipose tissue, indicating the dependence of radiotracer distribution volume on tissue composition. Osseous and lymph node metastases were significantly better perfused than local recurrences or reactive lymph nodes. Adipose tissue was the least well perfused, with k_3 values close to zero. A subanalysis of lesions categorized as local recurrences, lymph nodes, and osseous metastases is also included in Table 1. Despite similar SUVs between local recurrences and osseous metastases (4.00 ± 2.25 and 3.86 ± 1.24, respectively), a significant difference was observed in K_1 (0.49 ± 0.36 and 0.99 ± 0.92 min^{-1}, respectively; $P = 0.02$).

The Spearman ρ between lesion SUV and K_i^P was 0.94 (Fig. 1A), whereas that between lesion SUV and K_i^C was 0.91. A high correlation was observed between K_i^P and K_i^C (0.97) (Fig. 1B). A slight discrepancy between lesion K_i^P and K_i^C was mediated by K_1: the correlation between $\Delta(K_i^P\text{-}K_i^C)$ and K_1 was found to be −0.67. The discrepancy became more apparent for a K_i of 0.4 min^{-1} or greater (corresponding to an SUV ≥ ~6), indicating that the compartment model is not robust in these scenarios. Among the investigated kinetic rate constants, the correlation with SUV was the strongest for K_1 in all tissues (0.71), whereas for K_1/k_2 and k_3 it was 0.44 and 0.33 (Table 2). No correlation was found between lesion K_1 and k_3 ($\rho = -0.16$; $P = 0.09$); however, the correlation between K_1/k_2 and k_3 was −0.36 ($P < 0.01$). No significant correlation was observed between Gleason score or National Comprehensive Cancer Network score and any of the imaging metrics (i.e., SUV and kinetic rate constants). The Spearman ρ reached significance for correlations between PSA and SUV, K_i^P, and K_i^C (0.28, 0.26, and 0.21, respectively).

TABLE 1
Summary of ^{11}C-Choline Dynamic PET Analysis

Parameter	SUV	K_i^P (min^{-1})	K_i^C (min^{-1})	K_1 (min^{-1})	K_1/k_2	k_3 (min^{-1})	T* (min)
All prostate cancer lesions (n = 108)	3.60 ± 2.16 (0.82–12.00)	0.26 ± 0.17 (0.06–1.01)	0.28 ± 0.22 (0.07–1.33)	0.79 ± 0.98 (0.11–7.17)	2.92 ± 3.52 (0.31–20.00)	0.36 ± 0.30 (0.00–1.00)	9 ± 7
Local recurrences (n = 24)	4.00 ± 2.25 (1.75–8.96)	0.27 ± 0.13 (0.10–0.59)	0.26 ± 0.15 (0.11–0.68)	0.49 ± 0.36 (0.16–1.58)	3.37 ± 4.46 (0.46–20.00)	0.48 ± 0.33 (0.10–1.00)	9 ± 6
Lymph node metastases (n = 65)	3.40 ± 2.32 (0.82–12.00)	0.25 ± 0.19 (0.06–1.01)	0.26 ± 0.22 (0.07–1.33)	0.85 ± 1.17 (0.10–7.76)	2.49 ± 2.94 (0.06–12.39)	0.32 ± 0.27 (0.04–1.00)	9 ± 7
Osseous metastases (n = 19)	3.86 ± 1.24 (1.71–5.60)	0.31 ± 0.14 (0.11–0.68)	0.35 ± 0.20 (0.11–0.88)	0.99 ± 0.92 (0.16–3.37)	3.93 ± 4.11 (0.71–13.10)	0.39 ± 0.31 (0.05–1.00)	9 ± 7
Inflammatory lymph nodes (n = 60)	1.63 ± 0.70 (0.80–4.92)	0.11 ± 0.04 (0.06–0.26)	0.11 ± 0.04 (0.06–0.27)	0.34 ± 0.17 (0.10–0.95)	1.10 ± 0.58 (0.39–3.15)	0.21 ± 0.18 (0.06–1.00)	10 ± 5
Gluteus maximus muscle (n = 73)	1.02 ± 0.40 (0.43–2.02)	0.07 ± 0.03 (0.03–0.16)	0.13 ± 08 (0.04–0.31)	0.13 ± 0.08 (0.04–0.32)	1.34 ± 1.00 (0.32–5.71)	0.20 ± 0.11 (0.04–0.31)	20 ± 16
Adipose tissue (n = 73)	0.26 ± 0.07 (0.13–0.46)	0.02 ± 0.01 (0.01–0.10)	0.06 ± 04 (0.02–0.22)	0.07 ± 04 (0.02–0.29)	0.72 ± 0.27 (0.28–1.82)	0.03 ± 03 (0.00–0.18)	65 ± 69

Data are mean ± SD followed by range in parentheses.

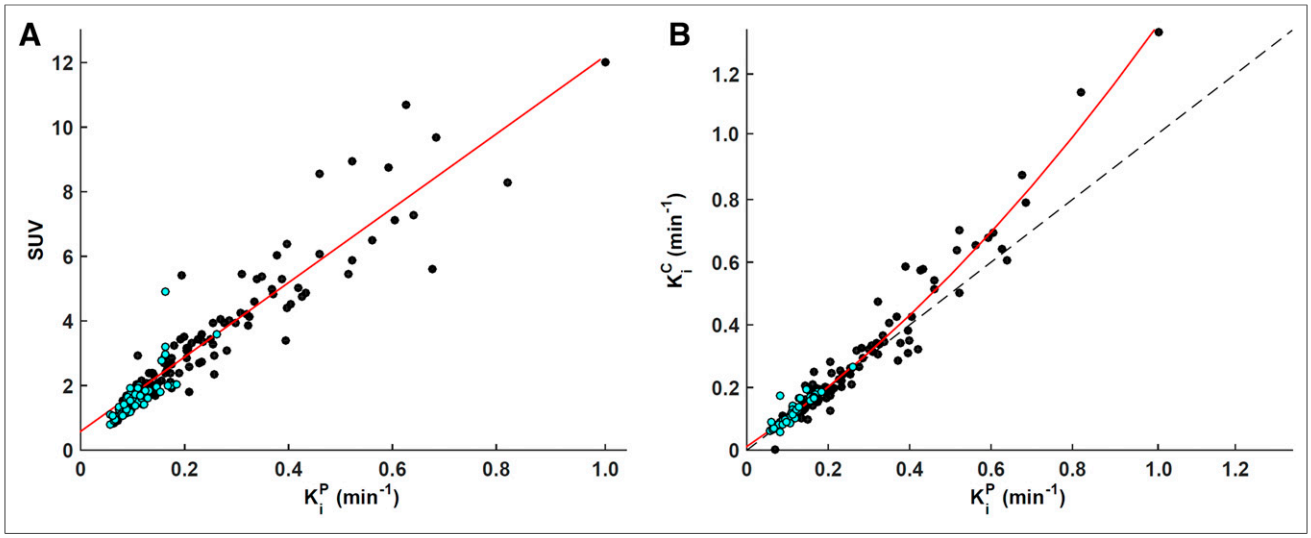

FIGURE 1. Population-wise comparison of ^{11}C-choline metrics derived from static and dynamic PET acquisitions. (A) Scatterplot of Patlak slope K_i^P (*x*-axis) vs. SUV (*y*-axis) for all lesions (black, $n = 108$, $\rho = 0.94$) and inflammatory lymph nodes (cyan, $n = 60$, $\rho = 0.93$). Regression slope = 11.5; regression intercept = 0.6. (B) Scatterplot of influx rate constant K_i as derived from graphical Patlak analysis (K_i^P, *x*-axis) and compartmental modeling (K_i^C, *y*-axis) for all lesions (black, $n = 108$, $\rho = 0.97$) and inflammatory lymph nodes (cyan, $n = 60$, $\rho = 0.96$). Second-degree polynomial fit and line of identity are shown as solid red line and dashed black line, respectively.

In 15% of the lesions for which 1-compartment models resulted in a lower Akaike information criterion value, fitting of time–activity curves was suboptimal regardless of the model used. This result was primarily due to a continuing gradual increase in tumor signal after an initial plateau was reached, as well as the suboptimal metabolite correction, which likely underestimated the radiotracer available for intracellular trapping (resulting in $k_3 \geq 0.4$ min^{-1}). When the analysis for all 108 lesions was repeated using input functions not corrected for metabolites, the quality of the fits improved substantially in the aforementioned 15% of lesions, and the 2T3K model was assessed as most appropriate in almost all cases. The correlations between SUV and K_i^P and between SUV and K_i^C were lower, however, at 0.83 and 0.80, respectively, whereas the corresponding correlations for K_1, K_1/k_2, and k_3 were 0.72, 0.67, and 0.31, respectively.

An example of both concordance and discordance between SUV and ^{11}C-choline pharmacokinetics is presented in Figure 2. In patient 1 (PSA, 8.6 ng/mL; Gleason score, 7), a metastatic lymph node with a higher SUV also exhibited a higher K_1 and K_1/k_2 (as well as a higher K_i^C; Fig. 2A). On the other hand, the 2 osseous metastases in patient 2 (PSA, 9.8 ng/mL; Gleason score, 8) exhibited markedly different kinetic rate constants despite having similar SUVs (Fig. 2B).

DISCUSSION

Compared with dynamic imaging, static PET scans are clinically more feasible, shorter, and better suited to a busy clinical schedule. However, our study indicated that similar SUVs can be produced by lesions exhibiting very different pharmacokinetics that reflect differences in tumor differentiation and perfusion. Nevertheless, a high correlation was observed between SUV and K_i as determined either by graphical Patlak analysis or by pharmacokinetic modeling, supporting the value of using the simpler static measure in place of dynamic PET scans to quantify ^{11}C-choline uptake in these patients for treatment monitoring.

Intracellular choline levels are determined both by the rate of choline uptake and by the rate of phosphatidylcholine synthesis and degradation. Experimental studies have indicated that a large fraction of the intracellular choline still represents nonmetabolized choline, suggesting that choline transport and not phosphorylation is the key factor in choline uptake by cancer cells (*17,18*). Henriksen et al. demonstrated that although tumor uptake of the choline derivative ^{18}F-deshydroxycholine—which cannot be phosphorylated by choline kinase—is similar to that of ^{11}C-choline at early time points (<5 min after injection), uptake of ^{11}C-choline is significantly higher at longer incubation times (>20 min after injection), because at earlier times radiolabel internalization is largely dependent on the choline transport rate whereas at later times choline phosphorylation becomes the dominant step in cellular enrichment (*19*).

The accumulation of ^{11}C-choline in tumors was rapid, as observed previously (*15,20,21*). In many cases, a plateau had already been reached within 1–3 dynamic 10-s frames. Among all investigated kinetic rate constants, K_1 correlated best with SUV. These

TABLE 2
Spearman ρ with SUV

Site	K_i^P	K_i^C	K_1	K_1/k_2	k_3
Prostate cancer lesions ($n = 108$)	0.94	0.91	0.70	0.44	0.33
Inflammatory lymph nodes ($n = 60$)	0.93	0.91	0.54	0.27	0.53
Gluteus maximus muscle ($n = 73$)	0.86	0.77	0.78	0.36	0.28
Adipose tissue ($n = 73$)	0.64	0.53	0.53	0.18*	0.41

*Significance not reached.

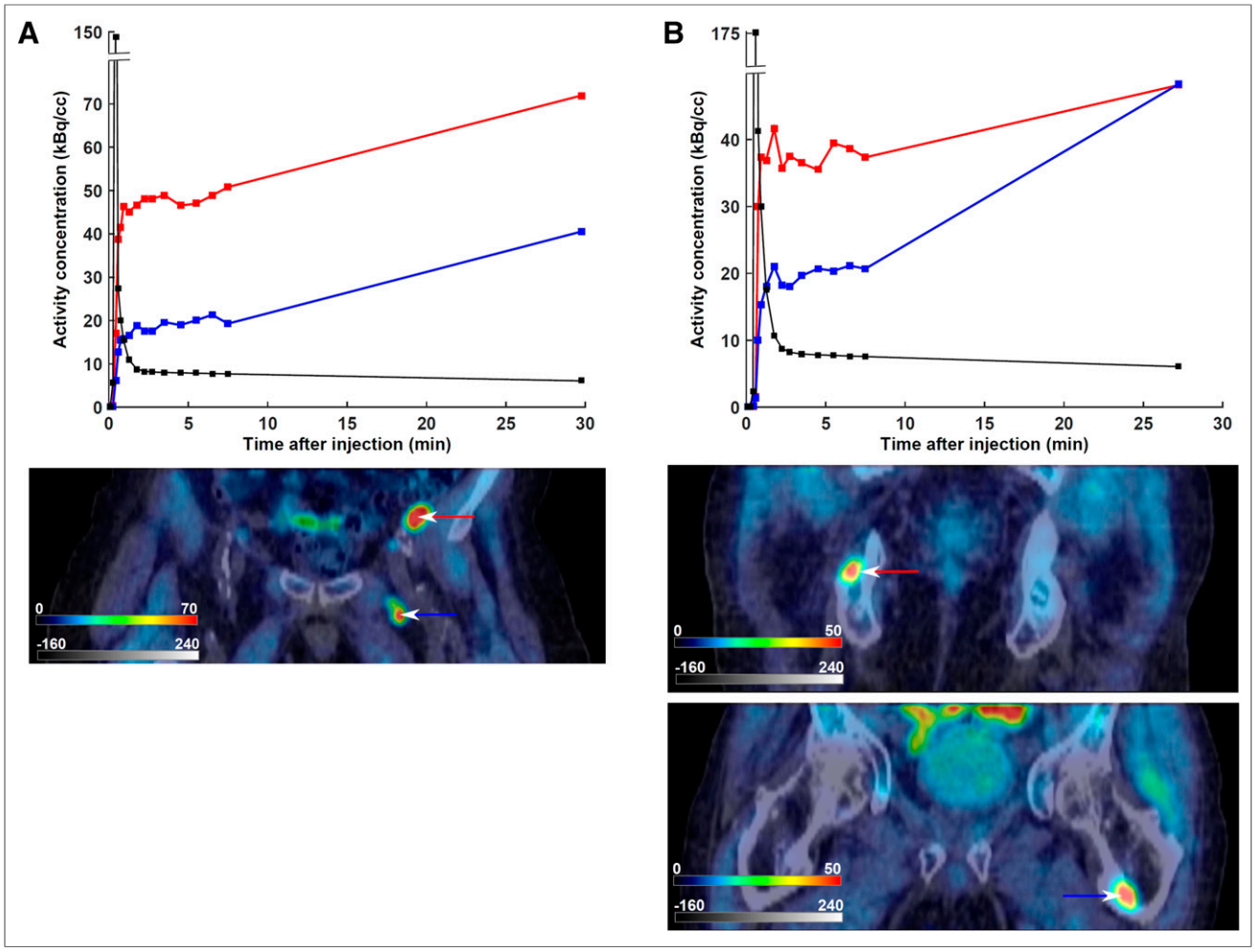

FIGURE 2. Relationship between SUV and ^{11}C-choline pharmacokinetics in 2 patients with biopsy-proven disease recurrence. Late static PET scans, fused with their corresponding CT scans, are included. Input function time–activity curves are superimposed in black. Color scales are kBq/cm^3 and Hounsfield units for PET and CT, respectively. (A) Patient 1, exhibiting concordance between SUV and kinetic rate constants. First lymph node, marked with red time–activity curve and arrow (SUV = 10.7, K_1 = 1.64 min^{-1}, K_1/k_2 = 4.91, k_3 = 0.21 min^{-1}), exhibits both higher SUV and higher K_1 and K_1/k_2 than second lymph node, marked with blue time–activity curve and arrow (SUV = 6.0, K_1 = 0.59 min^{-1}, K_1/k_2 = 1.16, k_3 = 0.70 min^{-1}). (B) Patient 2, exhibiting discordance between SUV and kinetic rate constants. The osseous metastasis marked with red time–activity curve and arrow (SUV = 5.0, K_1 = 0.97 min^{-1}, K_1/k_2 = 4.17, k_3 = 0.18 min^{-1}) has similar SUV but different pharmacokinetics from the osseous metastasis marked with blue time–activity curve and arrow (SUV = 5.0, K_1 = 0.41 min^{-1}, K_1/k_2 = 1.27, k_3 = 1.00 min^{-1}).

results are consistent with the foregoing observations if K_1 is taken to reflect not only tumor perfusion and vascular permeability but also the rate of choline transporter activity, whereas k_3 is assumed to reflect the irreversible and slower process of phosphorylation by choline kinase, which increases intracellular trapping of choline. In our study, K_1 and k_3 did not significantly correlate with each other. The preference of an irreversible 2-compartment model over other investigated models by the Akaike information criterion indicates that inclusion of the kinetic rate constant k_3 is preferable for describing ^{11}C pharmacokinetics.

Inaba has measured PCa blood flow using ^{15}O-water PET and reported that it averaged 15.7 mL/min/100 g (i.e., 0.157 min^{-1}, assuming unit density tissue), compared with 29.4 mL/min/100 g in PCa tissue (*22*). Subsequent studies confirmed that the average blood flow rate in PCa is approximately 2–3 times higher than in normal prostate (*23*). In the current study, comparison with normal prostate tissue was not possible since all patients underwent prostatectomy before ^{11}C-choline PET, although K_1 was about 3 times higher than values previously reported for normal prostate (Table 1) (*19,20*). Osseous and lymph node metastases were found to have still higher K_1 values than local recurrences (Table 1). PCa has a high propensity to metastasize to bone (*24*), specifically to the most heavily vascularized parts of the skeleton (*25*), and to stimulate osteoblast activity (*26*). This process is facilitated by the presence of adhesive molecules on tumor cells that bind them to marrow stromal cells, in turn increasing the production of angiogenic factors and bone-resorbing factors that enhance tumor growth (*27*). High perfusion of osteoblastic metastases has also been described using ^{18}F-NaF PET (*28*).

Analysis of time–activity curves revealed that in several cases, the activity concentration continued to gradually increase after an initial plateau was reached, in agreement with previous observations (*29*). Apart from free ^{11}C-choline and ^{11}C-phosphocholine, the tumor PET signal from ^{11}C-choline scanning also comprises the metabolite ^{11}C-betaine (an organic osmolyte produced in liver and kidneys), which contributes to the total uptake through

donation of the radiolabeled methyl group to L-homocysteine, producing radiolabeled L-methionine (*2*). Both ^{11}C-choline and ^{11}C-betaine enter the cells, albeit at different rates, which can conceivably vary between lesions. This process could in principle be modeled as a combined 4-tissue-compartment model, in which the tissue kinetics of both ^{11}C-choine and ^{11}C-betaine are described by 2 interlinked 2-tissue-compartment models. However, such a model requires more parameters than can reliably be fitted. There is also evidence that small amounts of ^{11}C-choline or its radioactive metabolites slowly accumulate in blood cells (*14,30*), introducing additional variability in how much of the measured ^{11}C activity concentration in blood is available for transport and intracellular trapping.

To the best of our knowledge, there has so far been only a single study of ^{11}C-choline pharmacokinetics in PCa—a study focusing on 14 patients with newly diagnosed disease (*20*). The authors reported a very high correlation between SUV and K_i as derived from graphical analysis (Pearson r = 0.96, $P < 0.01$), in agreement with our results. On the other hand, Verwer et al., investigating ^{18}F-fluoromethylcholine dynamic PET in 8 PCa patients, concluded that commonly used SUV metrics cannot be applied to quantify ^{18}F-fluoromethylcholine uptake reliably (*31*). The authors calculated K_1 from a 1T1K model (thus reflecting K_i) and reported an R^2 of 0.34 between SUV and K_1 (in our study, the corresponding R^2 was comparable, at 0.38). However, we found that a 1T1K was not the most appropriate model and that in most cases, a 2T3K model resulted in better fits. The authors also reported an R^2 of 0.58 between SUV and K_i^C (we observed a corresponding R^2 of 0.75), but the results of graphical analysis were not included (*32*). In another study—of ^{18}F-fluoroethylcholine dynamic PET in PCa patients (*32*)—the authors constrained K_1 to no more than 1 mL·min^{-1}·g^{-1} (Fig. 7A in 33); however, since K_1 does not have the same units as k_2 or k_3 (which represent fractions of mass transferred per unit time), physiologic values of K_1 can theoretically be above 1 mL·min^{-1}·g^{-1}. This possibility likely deteriorated the reported low correlation between SUV and K_1 (R^2 of 0.08).

^{11}C-choline uptake in inguinal lymph nodes was considered likely to represent inflammation (*13*). However, a limitation of our study was that disease recurrence could be confirmed for only 33 of 73 patients, because biopsies were not performed for the remaining patients. Another limitation was the absence of ^{11}C-choline metabolite analysis on a patient-by-patient basis, since arterial blood was not collected. Instead, a population-wise metabolite correction function, derived using previously published data (*14,15*), was multiplied by the patient's image-derived input function. In the foregoing studies, metabolism of ^{11}C-choline resulted in the fact that about 15% of the radioactivity present at 60 min after injection was due to ^{11}C-choline, with ^{11}C-betaine being the only observed radioactive metabolite. Patient-wise variability in metabolite fraction probably affected the quality of fitting but is not expected to have altered the interpretation of the results.

CONCLUSION

Our data represent the largest—to our knowledge—pharmacokinetic analysis of dynamic ^{11}C-choline PET scans on recurrent metastatic PCa. Our analysis showed that ^{11}C-choline pharmacokinetics in this setting were best described by the irreversible 2-compartment model. Malignant lymph nodes exhibited a higher SUV, as well as a higher K_i^P and K_i^C, than benign lymph nodes. Osseous metastases exhibited a higher blood flow than did local recurrences, despite having similar SUVs. Although pharmacokinetic modeling has potential to uncouple the contributions of different processes leading to entrapment of ^{11}C-choline within cancer cells, the high correlation between SUV and both K_i^P and K_i^C supports the use of a simpler SUV method to evaluate changes in ^{11}C-choline uptake and metabolism for treatment monitoring.

DISCLOSURE

This study was supported by Cancer Center Grant P30 CA008748 from NIH (principal investigator, Craig B. Thompson). No other potential conflict of interest relevant to this article was reported.

REFERENCES

1. Siegel RL, Miller KD, Jemal A. Cancer statistics, 2018. *CA Cancer J Clin.* 2018;68:7–30.
2. Zeisel SH. Dietary choline: biochemistry, physiology, and pharmacology. *Annu Rev Nutr.* 1981;1:95–121.
3. Bhakoo KK, Williams SR, Florian CL, Land H, Noble MD. Immortalization and transformation are associated with specific alterations in choline metabolism. *Cancer Res.* 1996;56:4630–4635.
4. Umbehr MH, Müntener M, Hany T, Sulser T, Bachmann LM. The role of ^{11}C-choline and ^{18}F-fluorocholine positron emission tomography (PET) and PET/CT in prostate cancer: a systematic review and meta-analysis. *Eur Urol.* 2013;64:106–117.
5. Evangelista L, Zattoni F, Guttilla A, et al. Choline PET or PET/CT and biochemical relapse of prostate cancer: a systematic review and meta-analysis. *Clin Nucl Med.* 2013;38:305–314.
6. Fanti S, Minozzi S, Castellucci P, et al. PET/CT with ^{11}C-choline for evaluation of prostate cancer patients with biochemical recurrence: meta-analysis and critical review of available data. *Eur J Nucl Med Mol Imaging.* 2016;43:55–69.
7. Ren J, Yuan L, Wen G, Yang J. The value of anti-1-amino-3-^{18}F-fluorocyclobutane-1-carboxylic acid PET/CT in the diagnosis of recurrent prostate carcinoma: a meta-analysis. *Acta Radiol.* 2016;57:487–493.
8. Evans JD, Jethwa KR, Ost P, et al. Prostate cancer-specific PET radiotracers: a review on the clinical utility in recurrent disease. *Pract Radiat Oncol.* 2018;8:28–39.
9. Schwenck J, Rempp H, Reischl G, et al. Comparison of ^{68}Ga-labelled PSMA-11 and ^{11}C-choline in the detection of prostate cancer metastases by PET/CT. *Eur J Nucl Med Mol Imaging.* 2017;44:92–101.
10. Hope TA, Truillet C, Ehman EC, et al. ^{68}Ga-PSMA-11 PET imaging of response to androgen receptor inhibition: first human experience. *J Nucl Med.* 2017;58:81–84.
11. Weber WA. Assessing tumor response to therapy. *J Nucl Med.* 2009;50(suppl 1):1S–10S.
12. Wahl RL, Jacene H, Kasamon Y, Lodge MA. From RECIST to PERCIST: evolving considerations for PET response criteria in solid tumors. *J Nucl Med.* 2009;50(suppl 1):122S–150S.
13. Ceci F, Castellucci P, Mapelli P, et al. Evaluation of prostate cancer with ^{11}C-choline PET/CT for treatment planning, response assessment, and prognosis. *J Nucl Med.* 2016;57(suppl 3):49S–54S.
14. Roivainen A, Forsback S, Grönroos T, et al. Blood metabolism of [methyl-^{11}C]choline: implications for in vivo imaging with positron emission tomography. *Eur J Nucl Med.* 2000;27:25–32.
15. Kenny LM, Contractor KB, Hinz R, et al. Reproducibility of [^{11}C]choline-positron emission tomography and effect of trastuzumab. *Clin Cancer Res.* 2010;16:4236–4245.
16. Akaike H. A new look at the statistical model identification. *IEEE Trans Automat Contr.* 1974;AC19:716–723.
17. Plathow C, Weber WA. Tumor cell metabolism imaging. *J Nucl Med.* 2008;49(suppl 2):43S–63S.
18. Bansal A, Shuyan W, Hara T, Harris RA, Degrado TR. Biodisposition and metabolism of [^{18}F]fluorocholine in 9L glioma cells and 9L glioma-bearing Fisher rats. *Eur J Nucl Med Mol Imaging.* 2008;35:1192–1203.

19. Henriksen G, Herz M, Hauser A, Schwaiger M, Wester HJ. Synthesis and preclinical evaluation of the choline transport tracer deshydroxy-[^{18}F]fluorocholine ([^{18}F]dOC). *Nucl Med Biol.* 2004;31:851–858.
20. Sutinen E, Nurmi M, Roivainen A, et al. Kinetics of [^{11}C]choline uptake in prostate cancer: a PET study. *Eur J Nucl Med Mol Imaging.* 2004;31:317–324.
21. Schaefferkoetter JD, Wang Z, Stephenson MC, et al. Quantitative ^{18}F-fluorocholine positron emission tomography for prostate cancer: correlation between kinetic parameters and Gleason scoring. *EJNMMI Res.* 2017;7:25.
22. Inaba T. Quantitative measurements of prostatic blood flow and blood volume by positron emission tomography. *J Urol.* 1992;148:1457–1460.
23. Vaupel P, Kelleher DK. Blood flow and oxygenation status of prostate cancers. In: Welch WJ, Palm F, Bruley DF, Harrison DK, eds. *Oxygen Transport to Tissue XXXIV. Advances in Experimental Medicine and Biology.* Vol 765. New York, NY: Springer; 2013:299–305.
24. Bubendorf L, Schöpfer A, Wagner U, et al. Metastatic patterns of prostate cancer: an autopsy study of 1,589 patients. *Hum Pathol.* 2000;31:578–583.
25. Gohji K, Kitazawa S. Molecular mechanism of prostate cancer invasion and metastasis. In: Mydlo JH, Godec CJ, eds. *Prostate Cancer: Science and Clinical Practice.* Cambridge, MA: Academic Press; 2003:11–28.
26. Charhon SA, Chapuy MC, Delvin EE, et al. Histomorphometric analysis of sclerotic bone metastases from prostatic carcinoma special reference to osteomalacia. *Cancer.* 1983;51:918–924.
27. Roodman GD. Mechanisms of bone metastasis. *N Engl J Med.* 2004;350:1655–1664.
28. Wong KK, Piert M. Dynamic bone imaging with ^{99m}Tc-labeled diphosphonates and ^{18}F-NaF: mechanisms and applications. *J Nucl Med.* 2013;54:590–599.
29. Contractor K, Challapalli A, Barwick T, et al. Use of [^{11}C]choline PET-CT as a noninvasive method for detecting pelvic lymph node status from prostate cancer and relationship with choline kinase expression. *Clin Cancer Res.* 2011;17:7673–7683.
30. Houck PR, Reynolds CF III, Kopp U, Hanin I. Red blood cell/plasma choline ratio in elderly depressed and demented patients. *Psychiatry Res.* 1988;24:109–116.
31. Verwer EE, Oprea-Lager DE, van den Eertwegh AJ, et al. Quantification of ^{18}F-fluorocholine kinetics in patients with prostate cancer. *J Nucl Med.* 2015;56:365–371.
32. Takesh M. Kinetic modeling application to ^{18}F-fluoroethylcholine positron emission tomography in patients with primary and recurrent prostate cancer using two-tissue compartmental model. *World J Nucl Med.* 2013;12:101–110.